Acoustic emission noise reduction: A case of a uniaxial compression test of gypsum-like rock

(Article begins on next page)

Acoustic emission noise reduction: a case of a uniaxial compression test of gypsum-like rock

Chongyang Wang[1,2], Dongming Zhang[1,2*], Ziyang Xiong[1,2], Beichen Yu[1,2], Xiaolei Wang[1,2], Fake Ren[1,2], Yu Chen[1,2]

1. State Key Laboratory of Coal Mine Disaster Dynamics and Control, Chongqing University, Chongqing 400030, China.

2. School of Resources and Safety Engineering, Chongqing University, Chongqing 400030, China.

** Correspondence: zhangdm@cqu.edu.cn.*

Abstract: In acoustic emission tests, the effective signal generated by crack initiation and propagation inside a sample is easily affected by the testing machine, earth vibration and other external noise, which increases the difficulty of data processing and analysis. To solve this problem, a gypsum sample under uniaxial compression is taken as an example to analyze and process the acoustic emission signal during the experiment. The test results show that these noises generally have the characteristics of acoustic sources far from the probe and signal types different from the effective signal. Therefore, a series of methods concerning the noise reduction of acoustic emission signals, including acoustic emission signal preprocessing, acoustic source distance denoising, and acoustic source type denoising, is proposed. Through three analyses and treatments of acoustic emission parameters, noise reduction was achieved with good results. According to the principles of these methods, some suggestions have been put forward for the position of probes in acoustic emission tests; that is, the connection of two probes should not be perpendicular to a weak plane (bedding, joints, etc.). These results could provide a theoretical reference for the postprocessing of acoustic emission signals in mechanical tests.

Keywords: Acoustic emission; Noise reduction; Acoustic source distance analysis; Acoustic source type analysis.

Highlights:

- A new method for determining noise signals by acoustic source distances is proposed.
- A new method for determining noise signals by acoustic type is proposed.
- Several suggestions were proposed for the position of the probe in the acoustic emission test.

1. Introduction

The phenomenon of releasing strain energy in the form of elastic waves is called acoustic emission when the material is deformed or cracked during stress. In mechanical tests, acoustic emission technology can be used to monitor the initiation, development and penetration of cracks. It is a very useful tool for experimental stress analysis (Schubnel et al., 2013; Okazaki et al., 2016; Ingraham et al., 2013; Qiao et al., 2022).

Many scholars at home and abroad have carried out many experimental studies using acoustic emission and analyzed the experimental results through signal processing (Choudhury et al., 2004; Zhang et al., 2015; Zhong et al., 2022; Hu et al., 2022; Meng et al., 2016; Lotidis et al., 2020; Kong et al., 2017). Harizi et al. (2022) proposed coupling three multivariate analysis techniques to apply acoustic emission data recorded on glass fiber-reinforced polymer composites to monitor and identify the damage mechanism in real time. Chai et al. (2022) studied the identification and prediction of fatigue crack growth in 316 LN stainless steel under different stress ratios by using acoustic emission technology to extract multiple acoustic emission parameters from acoustic emission waves and correlate acoustic emission signals with FCG under different load ratios. Van et al. (2022) used acoustic emission techniques to monitor damage caused by the corrosion of steel in RCs. A hierarchical clustering algorithm based on cross-correlation was developed and applied to automatically distinguish damage sources during the corrosion process. The algorithm can distinguish acoustic emission signals caused by corrosion, absorption, hydration and microcracks from those caused by macroscopic cracks. Gonzalez et al. (2022) proposed a new method based on deep learning using acoustic emission sensors to monitor grinding wheel wear status. Khazaei et al. (2015) studied the relationship between the total released acoustic energy and total consumed energy by specimens by analyzing real data and numerical models. Kudus et al. (2022) applied acoustic emission technology in structural health monitoring as a damage detection tool in material research and structural monitoring, expanding the ability and application of acoustic emission in damage detection strategies.

Many other scholars have used acoustic emission data to evaluate the failure characteristics of rocks and have reached meaningful conclusions (Mogi 1962; Scholz 1968; Liakopoulou et al., 1994; Lei et al., 2000; Thompson et al., 2006). Meredith et al. (1990) presented new results from a series of controlled laboratory experiments in which microseismic event rates and *b*-values were monitored contemporaneously with stress/time data for all variants of the stress/time relationship. Lockner et al. (1991, 1993) used a seismic location program to invert AE arrival time data to obtain the three-dimensional location of a microearthquake. Goebel et al. (2013) studied the change in the seismic *b*-value of AE events during stress accumulation and release in laboratory-made fault zones. The *b*-value reflects periodic stress changes that occur in a series of stick-slip events and is related to stress during many seismic cycles. Kwiatek et al. (2014) studied stick-slip events in western wind granite samples, revealing how differences in fault structure control the kinematics of microseismic activity during different periods of the seismic cycle. Liu et al. (2020a; 2020b) proposed a new method to estimate the *b*-value of acoustic emission tests of rocks and applied it to expansion fracture tests. The results show that the *b*-value is related to the heterogeneity and stress of the material. Chen et al. (2022) studied the attenuation effect of composite data generated from a double-truncated frequency–amplitude distribution and random sampling of known bottom b values on the estimation of *b*-values from a statistical point of view. The results showed that the determination of the minimum data size was influenced by the theoretical *b*-value of the bottom distribution.

However, in the process of acoustic emission testing, noise signals from the testing machine, the earth and other external sources are unavoidably detected. Therefore, many scholars have also conducted much research on noise processing technology during testing (Zhang et al., 2022; Habets et al., 2013; Zafar et al. 2021; Van et al., 2016; Redonnet et al., 2012; Wang et al., 2022b; Hassani et al., 2018). Dubbioso et al. (2022) proposed an active noise control strategy, which is achieved by limiting the absorbed power, load fluctuations and their combination. Prajna et al. (2019) proposed a Wiener filter to detect acoustic emission signals from a noisy environment. The algorithm is evaluated by means of the peak signal-to-noise ratio and mean square error. The performance of the proposed algorithm was demonstrated using simulated acoustic emission burst signals and acoustic emission signals acquired from compression tests and drilling tests. Dong et al. (2020a) established a seismic waveform image recognition model based on a convolutional neural network (CNN) to improve the efficiency and accuracy of microseismic data processing for monitoring rock instability and seismic activity. Moreover, they proposed a new acoustic emission location method that can locate microfracture sources and noise sources during uniaxial compression tests and provide more accurate sound source distance data (Dong et al., 2020b). He et al. (2020) proposed a new wavelet packet denoising method to weld acoustic emission signals. This method can be used to select effective acoustic emission functions according to the frequency distribution characteristics of welding crack acoustic emission signals and can effectively reduce the noise in welding crack acoustic emission signals. Tischmacher et al. (2011) presented several characteristic case studies of acoustic emission noise and examined the influence of diverse factors on the total noise level. Nguyen et al. (2015) proposed a robust condition monitoring methodology for rolling elements, which uses a new method to eliminate high noise in acoustic emission signals. Hussein et al. (2018) used a novel scheme of noise power spectrum density estimation to examine various types of acoustic emission signals. Synthetic and real data demonstrate the superiority of the proposed method over the wavelet shrinkage denoising method since it can more effectively eliminate white noise and preserve signals with a low signal-to-noise ratio.

Although many researchers have used various methods to reduce the noise of acoustic emission signals, such as signal filtering based on Fourier transform and signal wave model classification based on statistics (Vilhelm et al., 2008; Morales-Perez et al., 2022; Herzog et al., 2020), few studies have evaluated denoising methods based on acoustic source distance and type. In acoustic emission tests, common noise comes from the abnormal vibration generated during the loading process of the testing machine or from distant sound from the ground. The source of this noise is far from the probe relative to the sample. The longer propagation distance is far greater than the distance between the two acoustic emission probes, resulting in the difference in the intensity of the noise signal received by the two probes being smaller than the effective signal. In addition, the effective signal and noise have different timbres depending on the material, structure, and vibration mode. The strength of the signal changes the size of each parameter but does not affect the correlation between them. Therefore, in this paper, two new denoising methods, the source distance determination method and the source type determination method, are proposed. The acoustic emission parameters are denoised twice by using these two methods, and the acoustic emission data after denoising are obtained. Finally, according to the principle of the source distance determination method, some suggestions on the location of the probe in the acoustic emission test are proposed. This method has the advantages of simple operation, good noise reduction effect and no additional hardware equipment. This approach can provide a theoretical reference for reducing acoustic emission signal noise and determining the exact source location.

2. Acoustic emission signal and preprocessing

2.1 Introduction to acoustic emission signals

Figure 1 shows a schematic diagram of the acoustic emission signal parameters. In Figure 1, the ring-down count refers to the number of times that the sound wave exceeds the threshold, the energy represents the area between the signal crest line and the coordinate axis, the risetime represents the time from generation to the peak of the signal, and the duration indicates the total time needed for the signal to break the threshold voltage. The variable symbols are shown in Table 1.

Table 1. Acoustic emission parameters

Parameter	Time of arrival (s)	Risetime (μs)	Duration (ms)	Amplitude (mV)	Ring-down count	Energy (mV*ms)
Symbol	T_a	T_u	T_s	A	N	E

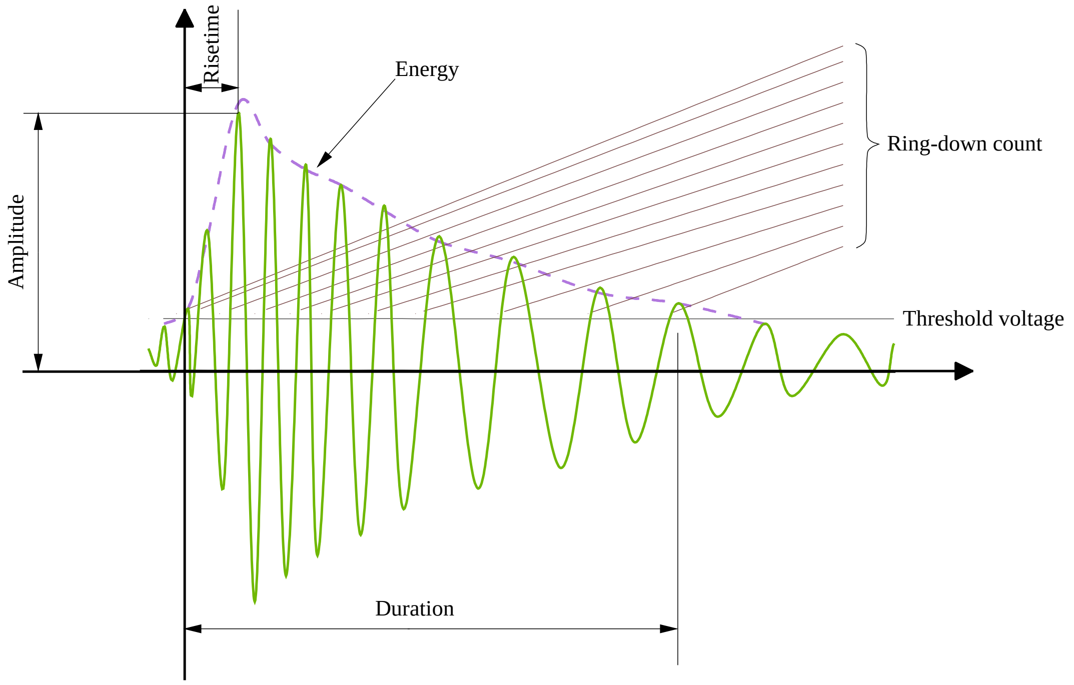

Figure 1. Schematic diagram of the acoustic emission signal parameters.

2.2 Source of signal

In this paper, we selected Grade A α-high-strength gypsum powder produced by the Sichuan Hongtai Company to prepare and pour standard cylindrical samples according to a mass ratio of distilled water to gypsum powder of 3:10. The sample size was Φ 50 mm × 100 mm. The specific preparation method of the sample is described previously (Wang et al., 2022a; 2023). After the sample was prepared, an electrohydraulic servo rock test system (RMT-150B; Figure 2a) and DS5-8B holographic acoustic emission signal analyzer (Figure 2c) were used to conduct a uniaxial compression test on the sample, and the acoustic emission data collected during the experiment were denoised. The displacement loading mode was adopted in the test, and the loading rate was 0.002 mm/s. In the test, the sampling frequency of the acoustic emission signal is 3 MHz, and the threshold value of the signal acquisition is 40 dB. Acoustic emission sensors were arranged on both sides of the bottom of the sample (Figure 2d), and the resonant frequency of the sensors was 150 kHz.

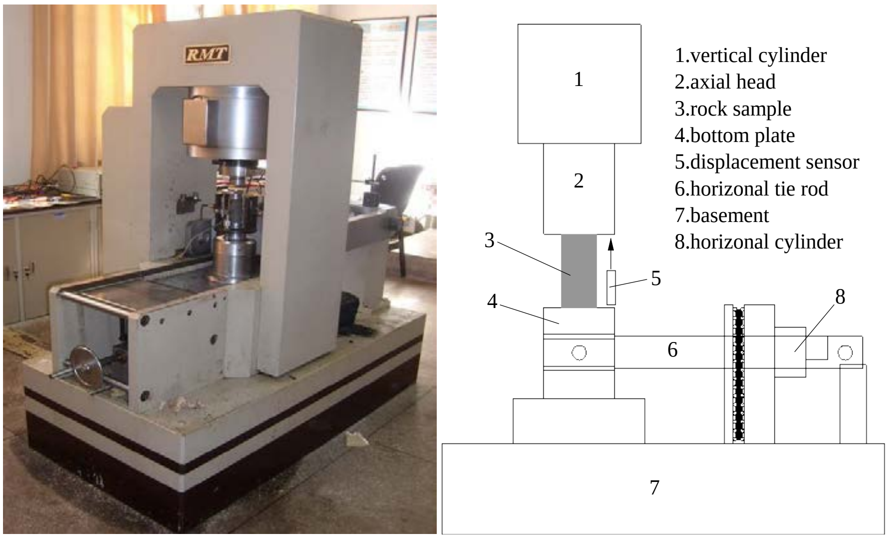

(a) (b)

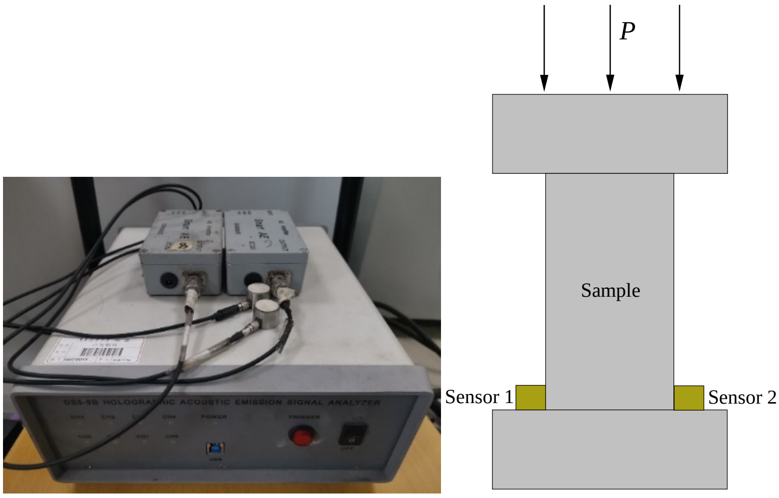

(c) (d)

Figure 2. Test equipment: (a) Electrohydraulic servo rock test system of RMT-150B. (b) Schematic diagram of uniaxial compression. (c) DS5-8B holographic acoustic emission signal analyzer. (d) Diagram of the sensor layout.

Figure 3 shows the stress–strain curve and acoustic emission signal variation curve of the sample under uniaxial compression. In Figures 3(b) and (c), the purple balls in three-dimensional space represent the ring-down count (N), while the cyan and pink balls are the projections of "N" on the (T_a, T_s) and (T_s, N) planes, respectively. The (T_a, T_s) plane extends in the negative direction along the T_s axis, and the graph drawn at T_s =-5 ms is the amplitude (A).

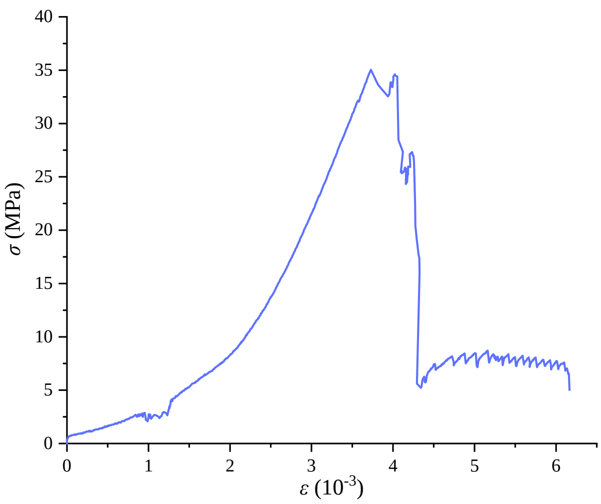

(a)

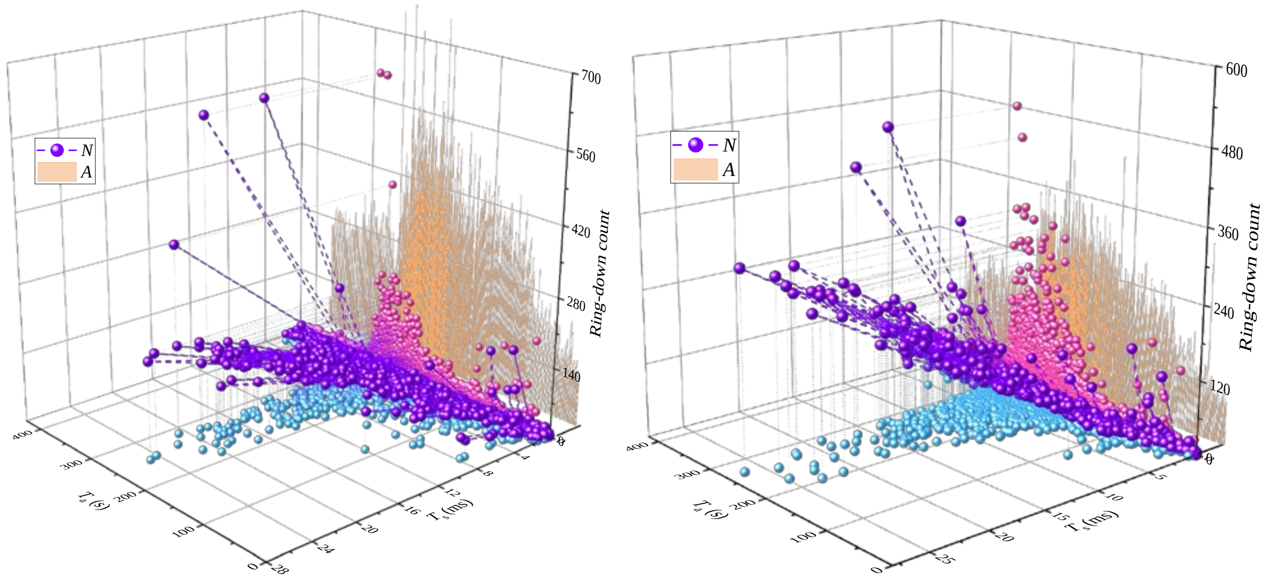

(b) (c)

Figure 3. Uniaxial compression test results for the gypsum sample: (a) stress–strain curve. (b) The acoustic emission signal in Channel 1. (c) Acoustic emission signal in Channel 2. {The purple balls in three-dimensional space represent the ring-down count (N), while the cyan and pink balls are the projections of "N" on the (T_a, T_s) and (T_s, N) planes, respectively.}

In the test, the two acoustic emission probes are placed at different positions (the specific locations of these two sensors are shown in Figure 1b), and the signals they receive will be different. Because the threshold voltage is set prior to the test, some minor vibrations may be captured by a single probe only. Therefore, it is necessary to preprocess the acoustic emission signals so that the signals received by the two probes correspond one by one.

The further away the same acoustic emission signal is from the probe, the lower its intensity will be when it reaches the probe. A change in the distance from the probe will result in a change in its amplitude, ring-down count, and other parameters. However, the risetime and duration of the signal wave change synchronously with the strength of the signal, and their ratios remain roughly unchanged (for isotropic samples, such as the gypsum-like rock used in this study). Therefore, both the "time of arrival" and "risetime/duration" factors can be used to determine the signal source. If the risetime/duration and time of arrival values are close to each other, the signals of two probes in sequence can be the same signal. A flow diagram of the signal preprocessing procedure is shown in Figure 4.

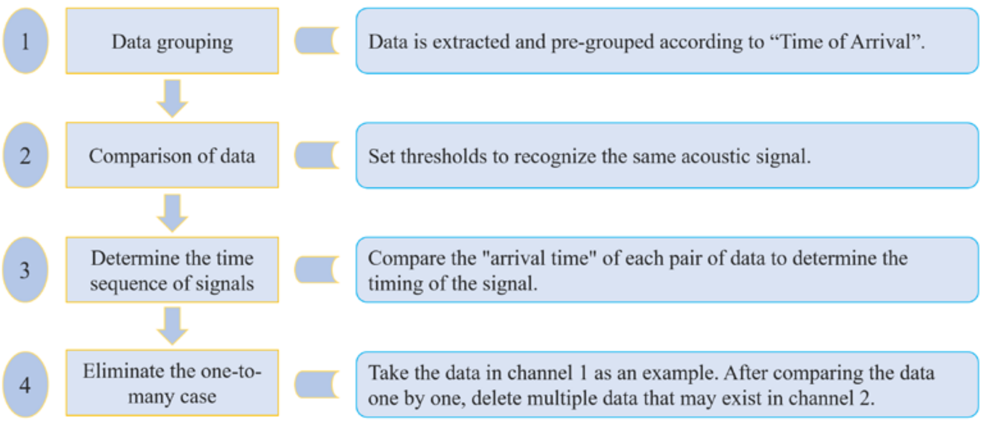

Figure 4. Flow chart of the signal preprocessing procedure.

2.3 Signal preprocessing

2.3.1 Data grouping

During data processing, the original acoustic signal data matrix was denoted A, and four columns of data, namely, the time of arrival and risetime/duration, of the two channels were extracted and stored in the new matrix B. By analyzing the acoustic emission parameters, the time of arrival changed between the two groups of acoustic signals (Figure 5), which can be regarded as the demarcation point between the two groups of acoustic signals.

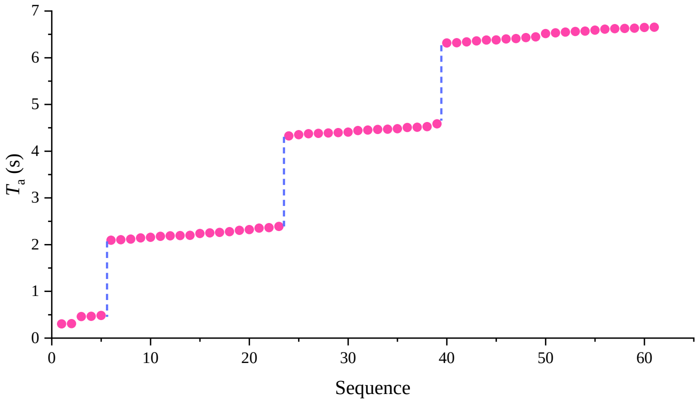

Figure 5. "Time of arrival" analysis of the two channel signals.

The threshold of the time of arrival was set to 0.5 s (the value must be less than the time difference at the group boundary point and greater than the time difference between signals in the same group), and the experimental data were grouped and stored in the 3D matrix s0 after processing. The third dimension of the s0 matrix represents different groups. By observing the 3D matrix after grouping, the signals whose difference in time of arrival between the groups was less than the threshold value were regarded as the same group of acoustic signals. The pseudocode for the data grouping is given in Algorithm 1.

Algorithm 1. Data grouping

Input: Time of arrival T_a, Risetime/duration T_r, Number of T_a r_T
Output: Grouped matrix *s0*
$\alpha \leftarrow 0$ and $\beta \leftarrow 0$
for $i \leftarrow 0$ to r_T-1 **do**
    $x_1 \leftarrow T_a[i]$ and $y_1 \leftarrow T_r[i]$
    $x_2 \leftarrow T_a[i+1]$ and $y_2 \leftarrow T_r[i+1]$
    if x_2-x_1<0.5 **then**
        $s0[\alpha, 1, \beta] \leftarrow x_1$
        $s0[\alpha, 2, \beta] \leftarrow y_1$
        $\alpha \leftarrow \alpha+1$
    else
        $\beta \leftarrow \beta+1$
        $\alpha \leftarrow 0$
    end if
    if x_2 is null **then**
        Jump out of this loop
    end if
end for
return *s0*

2.3.2 Comparison of the data

The threshold for the risetime/duration difference is set to 0.01, and the threshold for the time of arrival difference is set to 0.1 s. In the signals received by the two channels, if the difference between the two parameters is less than the threshold value, the difference is identified as the same acoustic signal. On this basis, matrix s0 is read sequentially. The first data of the left channel (Channel 1) are read first and compared with all the data of the right channel (Channel 2). If the above assumptions are met and both sets of data are not empty, this pair of data is stored in Matrix s1, after which the second data of the left channel are read and compared with all the data of the right channel. This process continues until all the data are matched. If the assumptions are not met, the algorithm will enter the next loop. The pseudocode corresponding to the acoustic signal is given in Algorithm 2.

Algorithm 2. Comparison of data

Input: Grouped matrix *s0*, Length of the third dimension of matrix s0 l_{s0}; Length of the first dimension of matrix s0 r_{s0}; "Risetime/Duration" of left and right channels (ε=1,2) r_ε; "Time of arrival" of left and right channels (ε=1,2)t_ε

Output: The sound signal corresponds to the preprocessed matrix *s1*

```
α←0 and β←0 and γ←0 and i←0
for δ←0 to l_s0-1 do
    for α←0 to r_s0-1 do
        for γ←0 to r_s0-1 do
            t2←s0[γ, 3, δ] and r2←s0[γ, 4, δ]
            t1←s0[α, 1, δ] and r1←s0[α, 2, δ]
            if |r2 − r1|< 0.01 and |t2 − t1|< 0.1 and r1 ≠ 0 and r2 ≠ 0 then
                if δ+1 ≠ i then
                    β←0
                end if
                n← [t1 r1 t2 r2]
                for η←0 to 3 do
                    s1[β, η, δ]←n[1, η]
                end for
                i←δ+1
                β←β+1
            end if
        end for
    end for
end for
return: s1
```

2.3.3 Determination of the time sequence of signals

With the same set of acoustic signals, if the rock failure location is closer to the left channel, the "time of arrival" of the left channel should be less than that of the right channel for all the data in the set, and vice versa. In Matrix s1 obtained by the above processing, the above factors are not considered.

We can define the count variables *fon*=0 and *beh*=0, traverse the grouping of Matrix s1, and compare the time of arrival of each pair of data. If the time of arrival of the left channel is longer than that of the right channel and the data are nonzero, then *fon* is increased by 1; in other cases, *beh* is increased by 1. If *fon* > *beh*, then all the data whose time of arrival in the left channel is longer than that in the right channel in this group are retained (as shown in Algorithm 3); if *beh* < *fon*, all the data whose time of arrival in the right channel is longer than that in the left channel in this group are retained (Reference Algorithm 3). Finally, the processed data are stored in Matrix s2.

Algorithm 3. Determine the chronological order

Input: The sound signal corresponds to the preprocessed matrix *s1*; Length of the first dimension of matrix s1 r_{s1}; Length of the third dimension of matrix s1l_{s1}

Output: Matrix after removing unreasonable chronological data *s2*

```
Π←0
for j←0 to l_s1 − 1 do
    for i←0 to r_s1 − 1 do
        if s1[i, 1, j] > s1[i, 3, j] and s1[i, 1, j] ≠ 0 and s1[i, 3, j] ≠ 0 then
            s2[Π, :]←s1[i, :, j]      //":" represents all data of the dimension
            Π←Π+1
        end if
    end for
end for
return: s2
```

2.3.4 Eliminating redundant data

After the above data processing, the signals of the two channels are roughly analyzed and sorted. However, a one-to-many situation will still occur. In viewing the data of the left channel, there may be multiple corresponding data points for the right channel after the above comparison. However, in actual situations, each pair of acoustic signal data should be unique. Therefore, risetime/duration is selected as the identification parameter of the acoustic signal, and the data corresponding to the "one-to-many" condition are compared. The data with the smallest absolute value of the difference between the risetime/duration are retained. We process the right channel data in the same way.

During the loop, because some data are culled, it is possible to traverse the data beyond the range of the array. Therefore, we place a zero matrix of the same size as a new s2 matrix under the original s2 matrix, and the new matrix is still named s2.

Taking the left channel as an example, the s2 matrix is traversed twice. If the left channel data read in the first traversal are the same as the left channel data read in the second traversal and the two-traversal data are not empty, the risetime/duration difference values of the two data points are compared, and the set of data with the smallest absolute value of the risetime/duration difference value is retained. The other set of data is deleted (as shown in Algorithm 4). The data obtained from the above processing steps are stored in the s3 matrix. Similarly, the right channel data were processed above, and the processed matrix was stored in the s4 matrix.

Algorithm 4. Eliminate the one-to-many case

Input: Length of the first dimension of the expanded new matrix s2r_{s2}

Output: Matrix after deleting one to many cases *s3*

for *i*←0 to $r_{s2}-1$ **do**
    for *k*←0 to $r_{s2}-1$ **do**
        if $i \neq k$ and *s2*[*i*, 1] = *s2*[*k*, 1] and *s2*[*i*, 1] ≠ 0 and *s2*[*k*, 1] ≠ 0 **then**
            if $|s2[i,2] - s2[i,4]| > |s2[k,2] - s2[k,4]|$ **then**
                Delete the data of *s2*[*i*,:]   //“ : ” represents all data of the dimension
            else
                Delete the data in *s2*[*k*,:]
            end if
        end if
    end for
end for
s3←*s2*
return: *s3*

2.3.5 Completing the data

The left and right channel data of the sound4 matrix and original data matrix A are traversed. If the data of a row of the sound4 matrix read are the same as those of a row in Matrix A, the other data of the row in sound4 will be filled, and the obtained matrix will be stored in the final matrix.

2.3.6 Pretreatment results

The preprocessed data are shown in Figure 5. As shown in Figure 6, after the above steps are preprocessed, the numbers of acoustic emission signals received by the two channels are completely consistent and can be compared one by one. This approach can meet the requirements of source distance denoising and source type denoising.

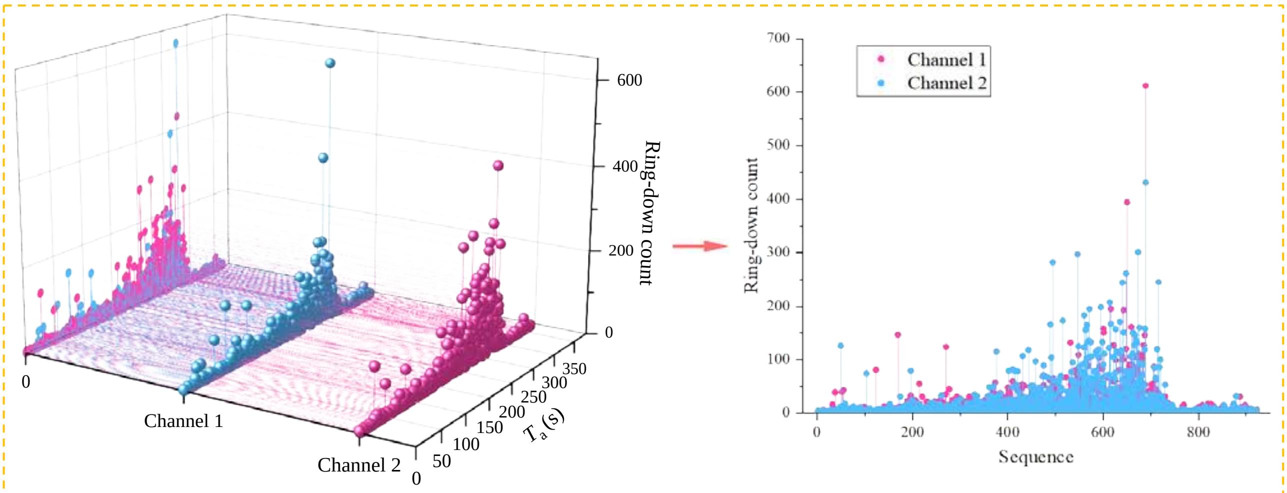

Figure 6. Preprocessing results of the acoustic emission signals.

3. Acoustic source distance denoising

3.1 Principle of the method

In acoustic emission tests, common noise comes from the abnormal vibration generated during the loading process of the testing machine or from distant sound from the ground and air. These noises have common characteristics; that is, the signal source is far from the probe relative to the sample. A longer propagation distance exceeds the distance between the two acoustic emission probes, resulting in a small difference in the intensity of the noise signals received by the two probes. As the acoustic emission probes are closely attached to the sample, the ratio of the time difference and travel time between the acoustic emission signals generated by the development and expansion of the new crack in the loading process to those of the two probes will increase (Figure 7).

As shown in Figure 7, it is assumed that the time from the internal signal of the sample to Probe 1 is t_1, and the time to Probe 2 is t_2. The time from the external signal to Probe 1 is t_1', and the time from the external signal to Probe 2 is t_2'. The relationships among these parameters are as follows:

$$\frac{t_1 - t_2}{t_1} \gg \frac{t_1{}' - t_2{}'}{t_1{}'} \tag{1}$$

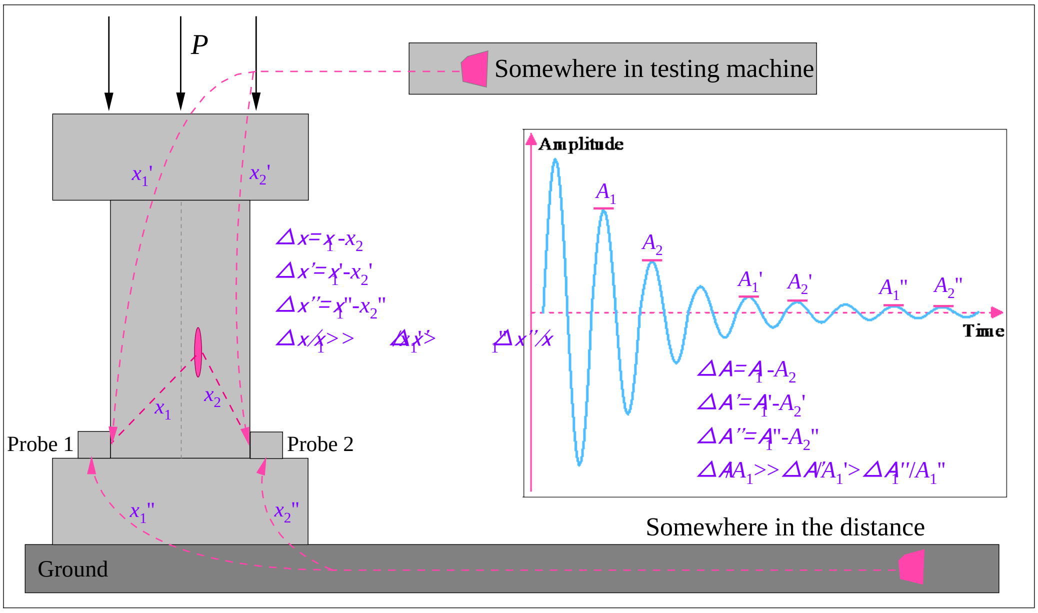

Figure 7. Schematic diagram of the noise reduction according to the acoustic source distance and signal intensity.

In addition, the propagation of the signal attenuates, and the attenuation speed is fast during the initial propagation and gradually decreases with increasing propagation distance. Therefore, signals generated in samples closer to the probe are more likely to show a difference in strength when they reach the two probes. However, there is no significant difference in the intensity of the acoustic source at longer distances.

It is assumed that the amplitude of Probe 1 that receives the internal signal of the sample is A_1 and that the amplitude of Probe 2 that receives the internal signal of the sample is A_2. Probe 1 receives external signals to Amplitude A_1', and Probe 2 receives external signals to Amplitude A_2'. The relationships among these parameters are as follows:

$$\frac{A_1 - A_2}{A_1} \gg \frac{A_1' - A_2'}{A_1'} \tag{2}$$

Therefore, the location of the signal source can be roughly determined according to the difference in the time and strength of the two probes that receive the signal. In other words, by setting threshold values, we can find the values of the approximate time of arrival and approximate intensity in the signal, which can be preliminarily determined as noise.

3.2 Noise reduction

According to the determination principle of the acoustic source distance in Section 3.1, we set the threshold value to η =10% to carry out the noise reduction processing of acoustic emission signals. First, the amplitude, ring-down count and energy are used to define the signal strength. The signal strength index λ is introduced and defined as a function of the amplitude, ringing count and energy:

$$\lambda \propto f(A, N, E) \tag{3}$$

In Equation (3), the amplitude is a one-dimensional parameter (length), the energy is a two-dimensional parameter (area), and the ring-down count is a statistical parameter. To unify the sign of the signal strength index λ, the energy is treated with the square root, and the imaginary number unit j is introduced to improve Equation (3):

$$\lambda = p + jq = f\left(A, \sqrt{E}\right) + j \cdot g(N) \tag{4}$$

The items in Equation (4) are as follows:

$$\begin{cases} f\left(A, \sqrt{E}\right) = xA + \sqrt{E} \\ g(N) = N \end{cases} \tag{5}$$

In Equation (5), x is a constant term. Introducing x brings the order of magnitude of A into line with that of $\sqrt{E}$. In this case, x is 0.1.

Then, Equation (4) can be written as:

$$\begin{cases} \lambda = 0.1A + \sqrt{E} + j \cdot N \\ |\lambda| = \sqrt{\left(0.1A + \sqrt{E}\right)^2 + N^2} \end{cases} \tag{6}$$

According to Equation (6), an image of the difference between the two channel signal intensity indices ($\triangle\lambda$) and ($\triangle|\lambda|$) was drawn, as shown in Figures 8 (a) and (b). Moreover, the time difference between the two channels receiving the same signal ($\triangle T_a$) was plotted, as shown in Figure 7(c).

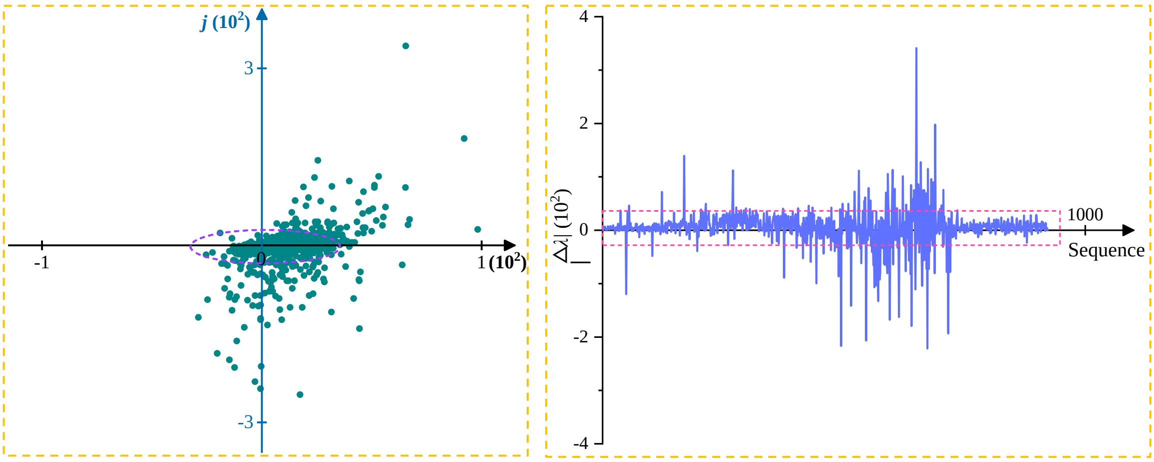

(a) (b)

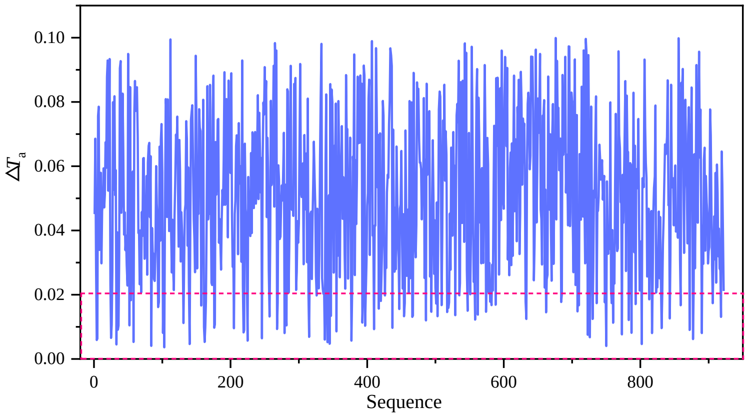

(c)

Figure 8. Acoustic emission signal denoising processing based on the acoustic source distance: (a) The difference between the two channel signal intensity indices (△λ). (b) The difference in the moduli of the two channel signal intensity indices (△ $|\lambda|$). (c) The time difference between the two channels receiving the same signal (△T_a).

In Figure 8, the dotted box represents the fraction below the threshold η. According to Chapter 2.2, if both the time of arrival and the intensity are close, it can be preliminarily determined to be noise. To find the parts satisfying the above conditions, $\triangle\lambda$ and $\triangle T_a$ are plotted on a function graph. The second imaginary number axis (*i*-axis) is introduced, and it is obtained by rotating the real number axis 90° around the origin in a plane perpendicular to the J-axis. Figure 9 (a) can be used as a reference to understand this principle. Thus, the determination function λ_p can be obtained:

$$\lambda_p = \triangle\left\{0.1A + \sqrt{E}\right\} + j\cdot\triangle N + i\cdot\triangle T_a \tag{7}$$

An image of λ_p is shown in Figure 9(b).

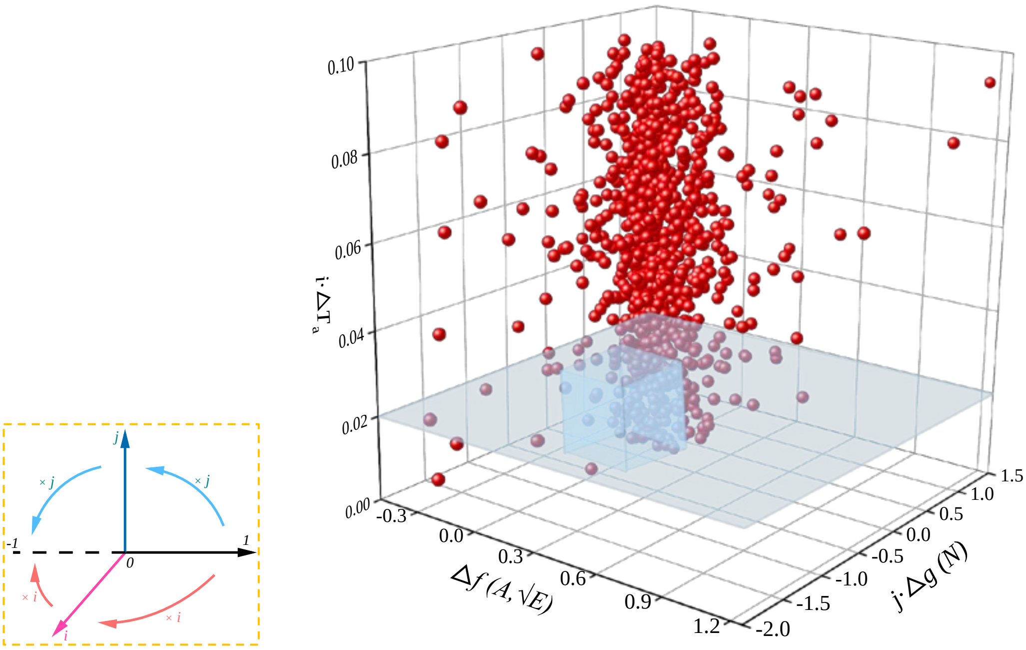

(a) (b)

Figure 9. Acoustic emission signal processing based on the acoustic source distance and intensity: (a) Diagram of the introduction of the *i*-axis. (b) Signal selection results.

The acoustic emission signal after noise reduction is shown in Figure 10.

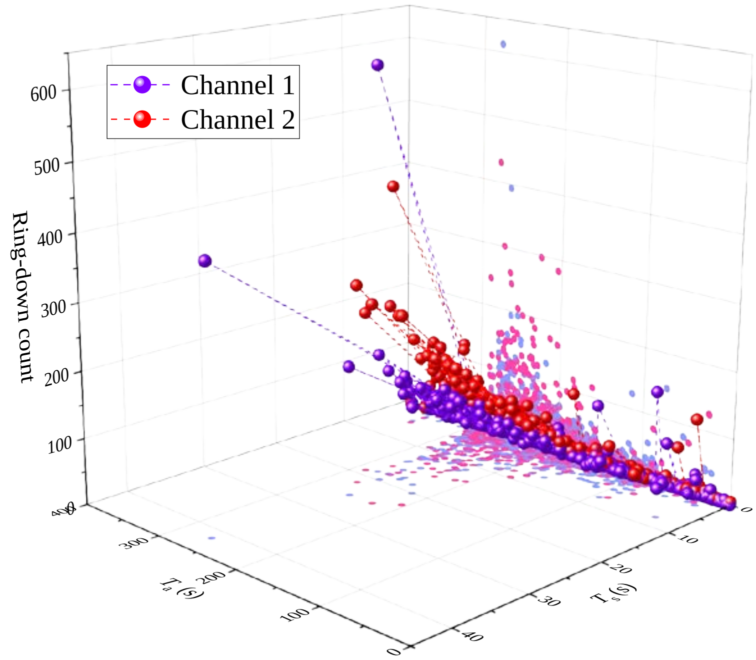

Figure 10. Acoustic emission signal processing results based on the acoustic source distance and signal intensity.

4. Acoustic source type denoising

4.1 Principle of the method

The closure and dislocation of the original cracks in the sample and the initiation, expansion and penetration of new cracks generate acoustic emission signals (Kim et al., 2015). In different stress stages, the evolution states of the cracks inside the sample differ, and the generated signal strength and duration also differ, which leads to changes in the amplitude and frequency of the signal wave (Chen et al., 2017; Xu et al., 2021).

However, in the same material, the vibrations produced by crack evolution have similar timbres. Due to the three factors that determine the timbre, the material, structure, and vibration mode are all similar. Therefore, there is a certain degree of correlation between the acoustic emission signals from inside rocks (such as the amplitude, ring-down count, energy, and duration). The strength of the signal changes the size of each parameter but does not affect the correlation between them. The signals from distant testing machine servo valves or ground vibrations are different because of the sound material and vibration mode, and the signal characteristics are obviously different from those of the signals inside the sample. Therefore, the difference between acoustic emission signal parameters can be used to distinguish signals from inside and outside the rock.

4.2 Noise reduction

According to the principle of determining the acoustic source type described in Chapter 2.3, the relationships among the duration, amplitude and energy of each acoustic emission signal are explored to define the signal type and construct a three-dimensional scatter diagram (see Figure 11).

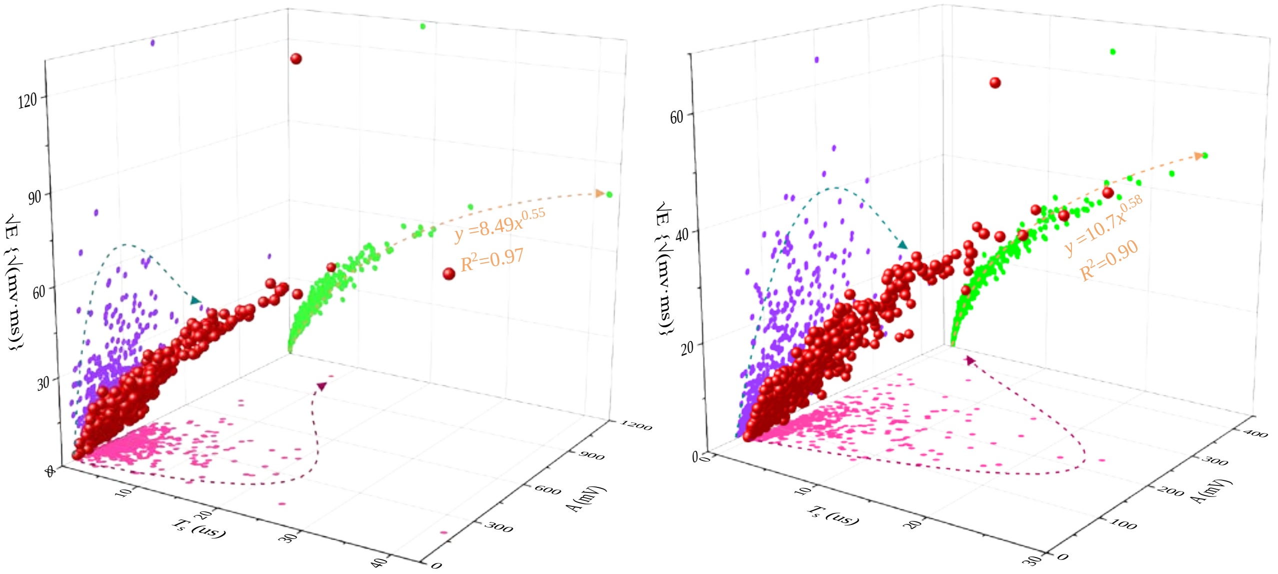

(a) (b)

Figure 11. Acoustic emission signal processing based on the acoustic source type: (a) Acoustic emission signal processing in Channel 1. (b) Acoustic emission signal processing in Channel 2.

As seen from the scatter plot in Figure 11 and its projections on all planes, $\sqrt{E}$ and T_s have strong regularity. With increasing T_s, $\sqrt{E}$ gradually increases, but the increase rate gradually decreases. The images in $\sqrt{E}$ and A show the characteristics of a centralized distribution, and the aggregation degree of the scattered points gradually decreases from zero to a positive direction. To further determine the relationship between the parameters, the scatter points in Figure 11 were projected on the ($\sqrt{E}$, T_s) and ($\sqrt{E}$, A) planes, as shown in Figure 12.

As shown in Figure 12(a), $\sqrt{E}$ and T_s are roughly exponential. The exponential function $y = ax^b$ is used to fit the $\sqrt{E}$-T_s curve, and the correlation coefficients of the scatter points of the two channels are both above 0.90. According to the principle of determining the acoustic source type, error analysis is carried out along the regression curve, the scattered points deviating from the curve are marked, and their abnormal points (the dots marked with light blue circular backgrounds in the figure and the same ones in the other figures) are removed. Figure 12(b) shows that the $\sqrt{E}$-A image changes from aggregation to divergence. The image points take (40,0) as the endpoints and gradually develop and diffuse in the first quadrant in the coordinate system {$\sqrt{E}$, A}. According to the principle of determining the acoustic source type, with (40,0) as the center of the circle, the density circle is drawn on the plane ($\sqrt{E}$, A), and the radius is a multiple of Amax. According to the coverage range of different density circles, the outliers far from the endpoints can be removed. Figure 13 shows the acoustic emission signal after noise reduction by source type.

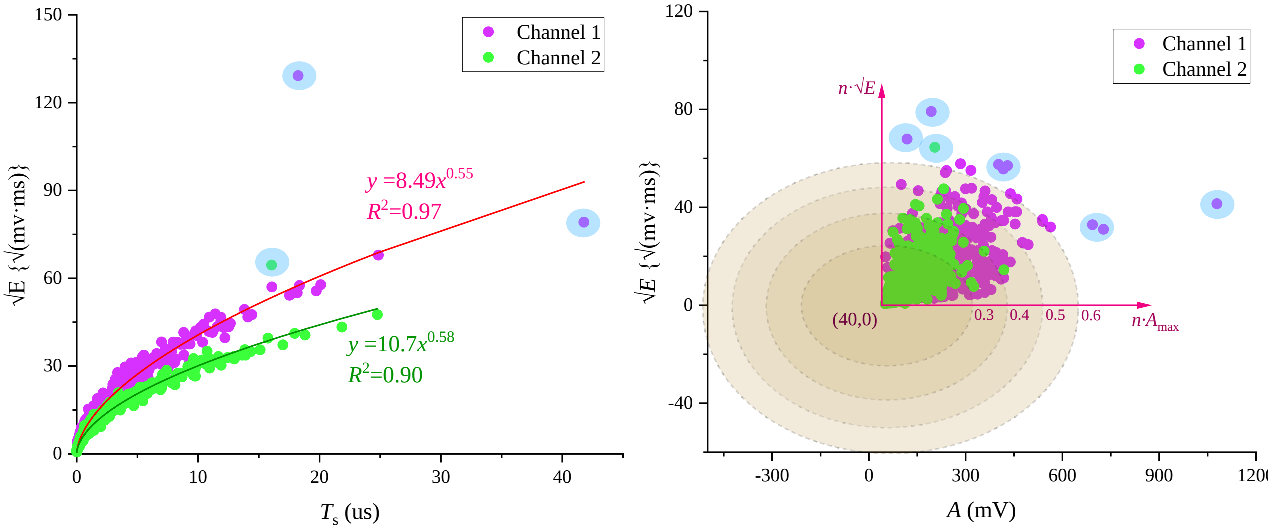

(a) (b)

Figure 12. Acoustic emission signal processing based on the acoustic source type: (a) $\sqrt{E}-T_s$ curve. (b) $\sqrt{E}-A$ curve.

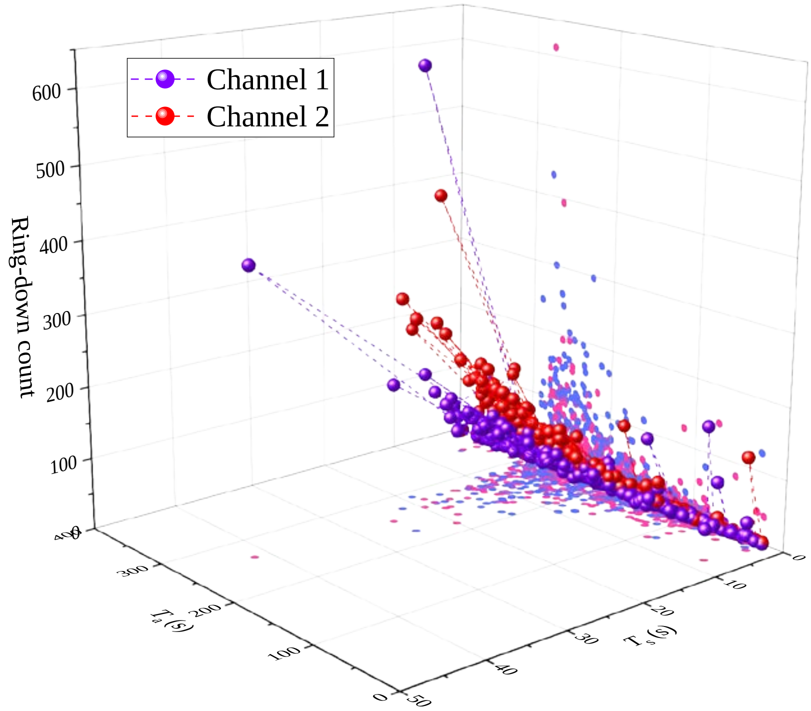

Figure 13. Acoustic emission signal processing results based on the acoustic source type.

5. Noise reduction results

By comparing the results in Figure 6, Figure 10 and Figure 13, it can be seen that after noise reduction processing based on the distance intensity and type of acoustic source, the dispersion degree of the acoustic emission signals of the sample gradually decreases, and the noise signals and anomalies are greatly reduced. To analyze the influence of the two noise reductions on the acoustic emission characteristics, a comparison diagram of the stress–strain curve and acoustic emission signals was drawn, as shown in Figure 14.

In Figure 14, the points circled by the green ellipse are the points eliminated after each noise reduction. Because of the large amount of data removed, only some obvious scatter points are identified. After the first noise reduction, 455 points were eliminated, and after the second noise reduction, 43 points were eliminated. After two noise reductions, the amount of acoustic emission noise is significantly reduced, and the recognition degree is greatly improved.

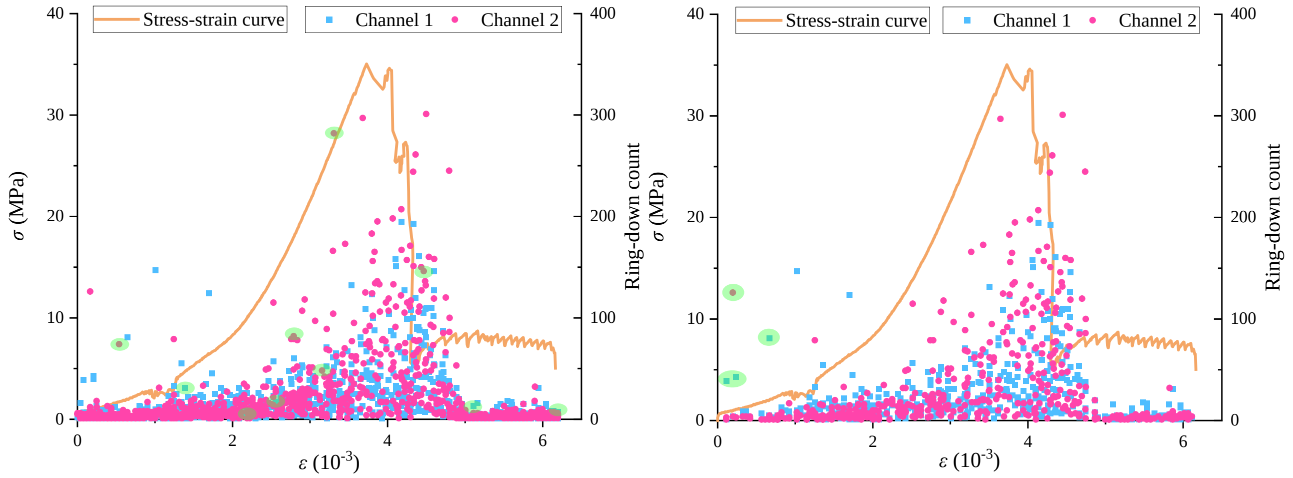

(a) (b)

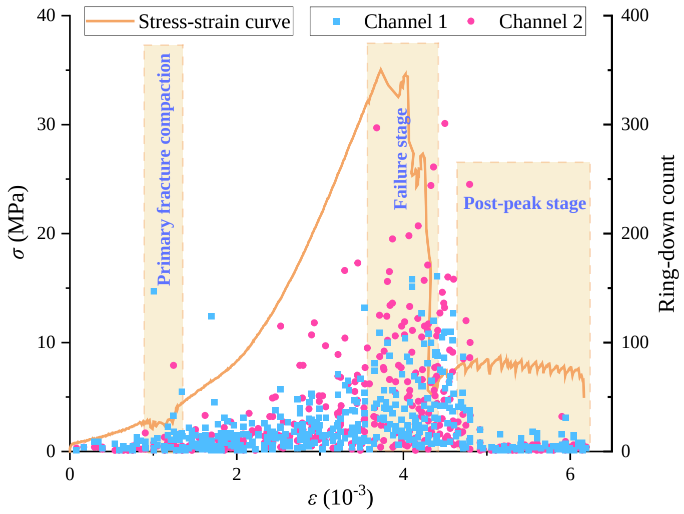

(c)

Figure 14. Analysis of the acoustic emission signal processing results: (a) Primary processing (acoustic source distance denoising). (b) Secondary processing (acoustic source type denoising). (c) Completion of processing.

By comparing Figures 14(a) and (b), in the compaction stage of the stress–strain curve, that is, at the beginning of the experiment, due to the initial unstable operation of the indenter of the testing machine and the preloading of the sample and the indenter, many "acoustic emission signals not from inside the sample" were generated. However, because the indenter is connected to the sample and the distance of the acoustic emission probe is close to the sample, the acoustic source distance processing method cannot be used to effectively identify such signals. Therefore, only a small part of the noise signal is removed in the first processing. However, the signals generated by the vibration of the indenter are obviously different from those emitted from the specimen due to the closure, development, and expansion of cracks. Therefore, the acoustic source type processing method can process the noise signal in this part well. As shown in Figure 14(c), the acoustic emission signals are relatively stable in the compaction stage, except that when the strain is 1‰, the sample generates louder emission signals due to internal fracture closure.

In addition to the compaction stage, in the other stages of the stress–strain curve, the recognition degree of the acoustic source distance treatment method is much greater than that of the acoustic source type treatment method, and the number of points removed by the former method is 10.6 times greater than that removed by the latter. This is because the acoustic source of the noise is generally far away, and the distance of the acoustic source weakens the difference in the acoustic source types, decreasing the difference in the acoustic emission parameters caused by different types of signals.

6. Discussion

6.1 Disadvantages and solutions of acoustic source distance denoising

The noise reduction method of the acoustic source distance in Section 2.2 can effectively eliminate acoustic emission signals that are far away from the sample, but there is a drawback: when the signal comes from the vertical bisector of the connection between two probes, the time of arrival at the two probes is very close, and this part of the signal is easily mistakenly deleted. As shown in Figure 15, when the sound point is transferred from Crack 1 to Crack 2, the distances between x_1 and x_2 tend to be equal. To avoid the use of the acoustic source distance processing method to identify these signals as distant noise signals and eliminate them, the analysis of the remaining characteristics of the signal should be increased. This is why we use source type processing for secondary noise reduction after source distance processing.

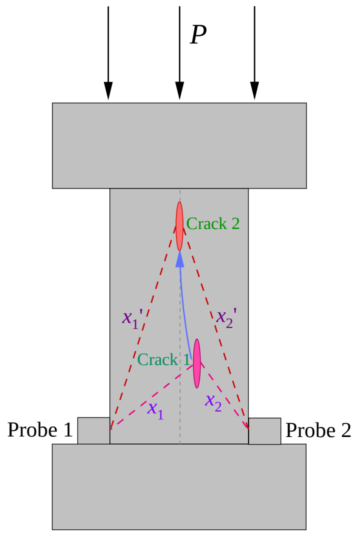

Figure 15. Relationship between the acoustic source position and signal travel time.

Figure 16 plots the propagation characteristics of acoustic signals at different times of arrival. As shown in Figure 16, when the position of the acoustic source is close to the probe, the probe will receive a signal with rapid amplitude decay. Due to the large amplitude decrease rate, the area (i.e., energy) enclosed by the peak envelope and threshold voltage is small. When the position of the acoustic source is far from the probe, the probe will receive the signal of a slow decrease in amplitude, and as the amplitude decrease rate is small, the energy will increase. Therefore, it is necessary to combine the source distance denoising method with the source type denoising method. When the sound signal reaches the probe, the acoustic source type processing method can be used to detect whether the sound signal is in the stage of rapid amplitude decline or slow amplitude decline to determine the position of the acoustic source and retrieve the signal points mistakenly deleted by the acoustic source distance processing method.

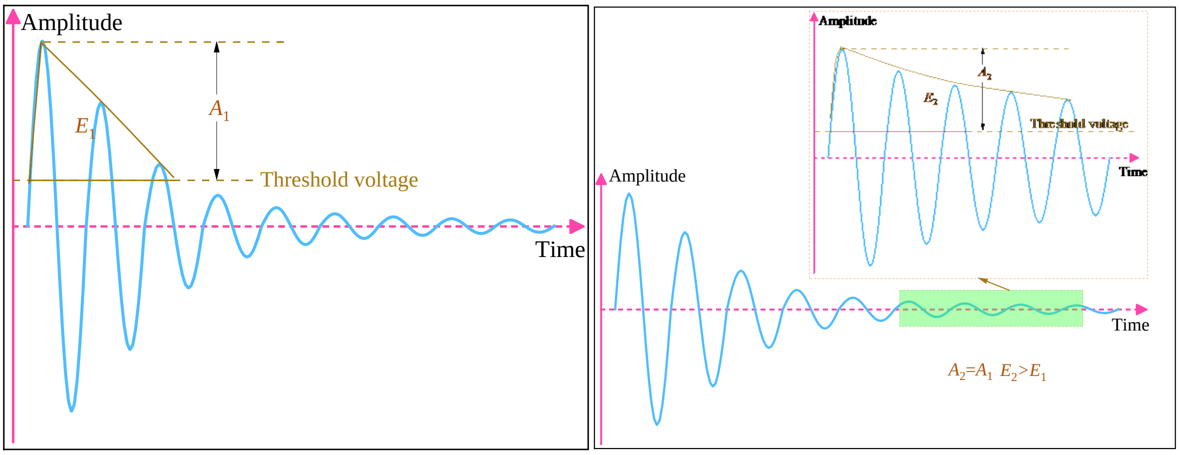

(a) (b)

Figure 16. Signal type and signal travel time: (a) Near range. (b) Long range.

6.2 Suitable probe arrangement

The source type denoising method can greatly avoid the error of the source distance denoising method. However, to further improve the accuracy of noise reduction and simplify the steps of noise reduction, the presence of too many acoustic sources on the vertical bisector of the line between two probes should be avoided during the acoustic emission test.

For example, in a mechanical test, when the maximum principal stress is parallel to a weak plane (joint or bedding), the sample will be destroyed by the lateral expansion of the weak plane. At this time, if the connection between the probes is perpendicular to the weak plane, the weak plane in the vertical bisector will cause the production of many signal points, which will be processed by the source distance denoising method. As shown in Figure 17, taking the cylindrical sample as an example (the same applies to the cubic sample), when the connection between the two probes is perpendicular to the sample bedding, the signal generated by the sample on the intermediate bedding is the same distance from the two probes. These signals are easily identified as noise by the acoustic source distance processing method, thus increasing the complexity of noise reduction processing. Therefore, when using this method for noise reduction analysis, we should try to avoid connecting probes perpendicular to the weak plane.

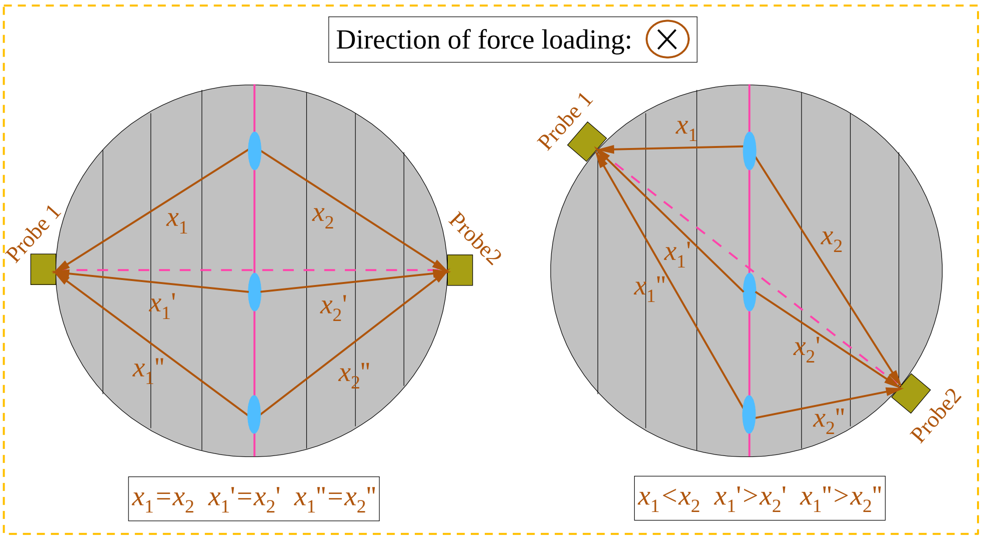

Figure 17. Influence of the arrangement of the probe on signal noise reduction.

7. Conclusions

In this paper, a series of methods for acoustic emission signal denoising, such as signal preprocessing, acoustic source distance denoising and acoustic source type denoising, are proposed and tested with examples. The conclusions are as follows:

1) In acoustic emission tests, the distance between common noise sources and acoustic emission probes is far greater than that between two probes, which results in differences in the duration and intensity of noise signals received by the two probes being smaller than the effective signals in the sample. Therefore, a method that determines the acoustic source distance is proposed to determine the noise signal by the time and intensity difference of the acoustic emission signal reaching two probes.

2) The effective signals from the interior of the rock exhibit a high degree of correlation between their parameters. The strength of the signal changes only the size of the parameters and does not affect the correlation between them. Due to the differences in the sound material and vibration mode, the signal characteristics of noise are obviously different from those of the effective signal. Thus, a method for determining noise signals by source type is proposed.

3) A total of 455 and 43 points were eliminated after noise reduction by acoustic source distance and type denoising, respectively. After two noise reductions, the number of acoustic emission signals is significantly reduced, and the recognition degree is greatly improved. The acoustic source distance determination method is the main noise reduction method, and the acoustic source type determination method is mainly aimed at the initial loading stage. The latter can complement and validate the former. The combination of the two methods has a good noise reduction effect.

4) In the acoustic emission test, when the connection of two probes is perpendicular to the specimen bedding, part of the acoustic emission signals generated by the specimen bedding expansion will be identified as noise signals, which will increase the complexity and reduce the accuracy of noise reduction processing. Therefore, when using this method for noise reduction, the connection between the probes should not be perpendicular to the weak surface.

8. Statements

8.1 Funding

This work was supported by the Scientific Research Foundation of the State Key Lab of Coal Mine Disaster Dynamics and Control. (Project Approval Number: 2011DA105287-zd201804)

8.2 Competing Interests

The authors have no relevant financial or nonfinancial interests to disclose.

8.3 Author Contributions

Dongming Zhang supervised the research and proposed this research direction. Chongyang Wang was responsible for the report analysis and writing of the paper. Ziyang Xiong was responsible for some of the data processing and literature research. Beichen Yu, Xiaolei Wang, Fake Ren and Yu Chen helped write the paper.

8.4 Data Availability

The datasets generated during and analyzed during the current study are available from the corresponding author upon reasonable request.

References

Chai M., Hou X., Zhang Z., Duan Q., 2022. Identification and prediction of fatigue crack growth under different stress ratios using acoustic emission data. *International Journal of Fatigue*. 160. http://doi.org/10.1016/j.ijfatigue.2022.106860.

Chen D., Liu X., He W., Xia C., Gong F., Li X., Cao X., 2022. Effect of attenuation on amplitude distribution and b-value in rock acoustic emission tests, *Geophysical Journal International*, 229(2), 933-947. https://doi.org/10.1093/gji/ggab480.

Chen Z., He C., Wu D., Xu G., Yang W., 2017. Fracture evolution and energy mechanism of deep-buried carbonaceous slate. *Acta Geotechnica*. 12(6), 1243-1260. http://doi.org/10.1007/s11440-017-0606-5.

Choudhury P., Raina A., Ramulu M., Chakraborty A., Bandopadhyay C., 2004. Crown pillar stability assessment in an underground copper mine using acoustic emission. *International Journal of Rock Mechanics and Mining Sciences*. 41(3), 399-400. http://doi.org/10.1016/j.ijrmms.2003.12.055.

Dong L., Tang Z., Li X., Chen Y. Xue J., 2020a. Discrimination of mining microseismic events and blasts using convolutional neural networks and original waveform, *Journal of Central South University*, 27(10): 3078-3089. http://doi.org/10.1007/s11771-020-4530-8.

Dong L., Hu Q., Tong X., Liu Y., 2020b. Velocity-Free MS/AE Source Location Method for Three-Dimensional Hole-Containing Structures, *Engineering*, 6(7): 827-834. http://doi.org/10.1016/j.eng.2019.12.016.

Dubbioso G., Muscari R., Ortolani F., Di Mascio A., 2022. Numerical analysis of marine propellers low frequency noise during maneuvering. Part II: Passive and active noise control strategies. *Applied Ocean Research*. 125. http://doi.org/10.1016/j.apor.2022.103201.

Goebel T., Schorlemmer D., Becker T., Dresen G., Sammis C., 2013. Acoustic emissions document stress changes over many seismic cycles in stick-slip experiments, *Geophysical Research Letters*, 40, 2049-2054. https://doi.org/10.1002/grl.50507.

González D., Alvarez J., Sánchez J. A., Godino L., Pombo I., 2022. Deep learning-based feature extraction of acoustic emission signals for monitoring wear of grinding wheels. *Sensors*. 22(18). http://doi.org/10.3390/s22186911.

Habets E., Benesty J., 2013. Multi-microphone noise reduction based on orthogonal noise signal decompositions. *IEEE Transactions on Audio Speech and Language Processing*. 21(6), 1123-1133. http://doi.org/10.1109/TASL.2013.2244086.

Harizi W., Chaki S., Bourse G., Ourak M., 2022. Damage mechanisms assessment of Glass Fiber-Reinforced Polymer (GFRP) composites using multivariable analysis methods applied to acoustic emission data. *Composite Structures*. 289. http://doi.org/10.1016/j.compstruct.2022.115470.

Hassani H., Hlousek F., Alexandrakis C., Buske S., 2018. Migration-based microseismic event location in the Schlema-Alberoda mining area, International Journal of Rock Mechanics and Mining Sciences, 110: 161-167. http://doi.org/10.1016/j.ijrmms.2018.08.002.

He K., Xia Z., Si Y., Lu Q., Peng Y., 2020. Noise reduction of welding crack AE signal based on emd and wavelet packet. *Sensors*. 20(3). http://doi.org/10.3390/s20030761.

Herzog A., Habets E., 2020. Direction and reverberation preserving noise reduction of ambisonics signals. *IEEE-*

Acm Transactions on Audio Speech and Language Processing. 28, 2461-2475. http://doi.org/10.1109/TASLP.2020.3013979.

Hu C., Mei F., Hussain W., 2022. Wavelet energy evolution characteristics of acoustic emission signal under true-triaxial loading during the rockburst test. *Applied Sciences*. 12(15). http://doi.org/10.3390/app12157786.

Hussein R., Shaban K., El-Hag A., 2018. Denoising different types of acoustic partial discharge signals using power spectral subtraction. *High Voltage*. 3(1): 44-50. http://doi.org/10.1049/hve.2017.0119.

Ingraham M., Issen K., Holcomb D., 2013. Use of acoustic emissions to investigate localization in high-porosity sandstone subjected to true triaxial stresses. *Acta Geotechnica*. 8(6), 645-663. http://doi.org/10.1007/s11440-013-0275-y.

Khazaei C., Hazzard J., Chalaturnyk R., 2015. Damage quantification of intact rocks using acoustic emission energies recorded during uniaxial compression test and discrete element modeling. *Computers and Geotechnics*. 67, 94-102. http://doi.org/10.1016/j.compgeo.2015.02.012.

Kim J., Lee K., Cho W., Choi H., Cho G., 2015. A comparative evaluation of stress-strain and acoustic emission methods for quantitative damage assessments of brittle rock. *Rock Mechanics and Rock Engineering*. 48(2), 495-508. http://doi.org/10.1007/s00603-014-0590-0.

Kong B., Wang E., Li Z., Wang X., Chen L., Kong X., 2017. Nonlinear characteristics of acoustic emissions during the deformation and fracture of sandstone subjected to thermal treatment. *International Journal of Rock Mechanics and Mining Sciences.* 90, 43-52. http://doi.org/10.1016/j.ijrmms.2016.10.004.

Kudus S., Bunnori N., Mustaffa N., Jamadin A., 2022. Investigation on acoustic emission parameters due to fatigue damage of concrete beams with variable notched depth. *International Journal of Concerete Structures and Materials*. 16(1). http://doi.org/10.1186/s40069-022-00518-8.

Kwiatek G., Goebel T., Dresen G., 2014. Seismic moment tensor and b-value variations over successive seismic cycles in laboratory stick-slip experiments. *Geophysical Research Letters*, 41, 5838-5846. https://doi.org/10.1002/2014GL060159.

Lei X., Kusunose K., Nishizawa O., Cho A., Satoh T., 2000. On the spatio-temporal distribution of acoustic emissions in two granitic rocks under triaxial compression: the role of pre-existing cracks, Geophys. *Geophysical Research Letters*, 27, 1997-2000. https://doi.org/10.1029/1999GL011190.

Liakopoulou F., Main I., Crawford B., Smart B., 1994. Microseismic properties of a homogeneous sandstone during fault nucleation and frictional sliding. *Geophysical Journal International*, 119(1), 219-230. https://doi.org/10.1111/j.1365-246X.1994.tb00923.x.

Liu X., Liu Z., Li X., Gong F., Du K., 2020a. Experimental study on the effect of strain rate on rock acoustic emission characteristics. *International Journal of Rock Mechanics and Mining Sciences*, 133. https://doi.org/10.1016/j.ijrmms.2020.104420.

Liu X., Han M., He W., Li X., Chen D., 2020b. A New b-value Estimation Method in Rock Acoustic Emission Testing, *Journal of Geophysical Research: Solid Earth*, 125, e2020JB019658. https://doi.org/10.1029/2020JB019658.

Lockner D., Byerlee J., Kuksenko V., Ponomarev A., Sidorin A., 1991. Quasi-static fault growth and shear fracture energy in granite. *Nature*, 350, 39-42. https://doi.org/10.1038/350039a0.

Lockner D., 1993. The Role of Acoustic Emission in the Study of Rock Fracture, International *Journal of Rock Mechanics and Mining Sciences & Geomechanics Abstracts*, 30(7), 883~899. https://doi.org/10.1016/0148-9062(93)90041-B.

Lotidis M., Nomikos P., Sofianos A., 2020. Laboratory study of the fracturing process in marble and plaster hollow plates subjected to uniaxial compression by combined acoustic emission and digital image correlation techniques. *Rock Mechanics and Rock Engineering*. 53(4), 1953-1971. http://doi.org/10.1007/s00603-019-02025-x.

Meng Q., Zhang M., Han L., Pu H., Nie T., 2016. Effects of acoustic emission and energy evolution of rock specimens under the uniaxial cyclic loading and unloading compression. *Rock Mechanics and Rock*

Engineering. 49(10), 3873-3886. http://doi.org/10.1007/s00603-016-1077-y.

Meredith P., Main I., 1990. Temporal variations in seismicity during quasi-static and dynamic rock failure. *Tectonophysics*, 175(1), 249-268. https://doi.org/10.1016/0040-1951(90)90141-T.

Mogi K., 1962. Study of the elastic shocks caused by the fracture of heterogeneous materials and its relations to earthquake phenomena. *Bulletin Earthquake Research Institute*, 40, 125-173.

Morales-Perez C., Rangel-Magdaleno J., Peregrina-Barreto H., Garcia-Perez A., Ramirez-Cortes JM., 2022. Noise reduction in electrical signal using OMP algorithm based on DCT and DSC dictionaries. *IEEE Transactions on Instrumentation and Measurement*. 71, 6500811. http://doi.org/10.1109/TIM.2021.3135319.

Nguyen P., Kang M., Kim J., Ahn B., Ha J., Choi B., 2015. Robust condition monitoring of rolling element bearings using de-noising and envelope analysis with signal decomposition techniques. *Expert Systems with Applications*, 42(22): 9024-9032. http://doi.org/10.1016/j.eswa.2015.07.064.

Okazaki K., Hirth G., 2016. Dehydration of lawsonite could directly trigger earthquakes in subducting oceanic crust. *Nature*. 530(7588), 81-+. http://doi.org/10.1038/nature16501.

Prajna K., Mukhopadhyay C., 2019. Efficient harmonic regeneration noise reduction-based Wiener filter for acoustic emission signal detection. *Electronics Letters*. 55(22):1163. http://doi.org/10.1049/el.2019.2196.

Qiao C., Song Z., Wang Y., Tannant D., Li C., 2022. Fractures and acoustic emission features of non-persistent jointed rocks subjected to freeze-thaw-compression load: experimental insights. *Rock Mechanics and Rock Engineering*. 55(1), 109-123. http://doi.org/10.1007/s00603-021-02667-w.

Redonnet S., Druon Y., 2012. Computational aeroacoustics of aft fan noises characterizing a realistic coaxial engine. *AIAA Journal*. 50(5): 1029-1046. http://doi.org/10.2514/1.J050730.

Scholz C., 1968. The frequency-magnitude relation of microfracturing in rock and its relation to earthquakes. *Bulletin of the Seismological Society of America*, 58(1), 399-415. http://doi.org/10.1785/BSSA0580010399.

Schubnel A., Brunet F., Hilairet N., Gasc J., Wang Y., Green H., 2013. Deep-focus earthquake analogs recorded at high pressure and temperature in the laboratory. *Science*. 341(6152), 1377-1380. http://doi.org/10.1126/science.1240206.

Thompson B., Young R., Lockner D., 2006. Fracture in Westerly granite under AE feedback and constant strain rate loading: Nucleation, quasi-static propagation, and the transition to unstable fracture propagation, *Pure and Applied Geophysics*, 163, 995-1019. https://doi.org/10.1007/s00024-006-0054-x.

Tischmacher H., Tsoumas I., Eichinger B., Werner U., 2011. Case studies of acoustic noise emission from inverter-fed asynchronous machines. *IEEE Transactions on Industry Applications*. 47(5): 2013-2022. http://doi.org/10.1109/TIA.2011.2161740.

Van H., Yoon J., He D., 2016. Low speed bearing fault diagnosis using acoustic emission sensors. *Applied Acoustics*, 105: 35-44. http://doi.org/10.1016/j.apacoust.2015.10.028.

Van S., Verstrynge E., 2022. Signal-based acoustic emission clustering for differentiation of damage sources in corroding reinforced concrete beams. *Applied Science*s, 12(4). http://doi.org/10.3390/app12042154.

Vilhelm J., Rudajev V., Lokajicek T., Zivor R., 2008. Application of autocorrelation analysis for interpreting acoustic emission in rock. *International Journal of Rock Mechanics and Mining Sciences*. 45(7), 1068-1081. http://doi.org/10.1016/j.ijrmms.2007.11.004.

Wang C., Wei S., Pan Y., Zhang S., 2022a. Experimental study on fatigue life of gypsum-like rock under uniaxial compression with different loading frequencies. *Pure and Applied Geophysics*. 179(4), 1225-1239. https://doi.org/10.1007/s00024-022-02966-5.

Wang C., Wei S., Zhang D., Yang Y., Yu B., Pan Y., 2023. Physical properties and tensile strength evolution of gypsum materials under different water content conditions. *Construction and Building Materials*. 364. https://doi.org/10.1016/j.conbuildmat.2022.129865.

Wang X., Zhu G., Cheng D., Miao B., Chen F., Tian H., 2022b. Spatiotemporal evolution characteristics of apparent resistivity and its response correlation with acoustic emission of coal under multi-step loading. *Sustanability*.14(16). http://doi.org/10.3390/su141610061.

Xu G., Hu X., Tang R., Hou Z., 2021. Fracture evolution of transversely isotropic rocks with a pre-existing flaw under compression tests based on moment tensor analysis. *Acta Geotechnica*. 17(1), 169-203. http://doi.org/10.1007/s11440-021-01214-9.

Zafar T., Kamal K., Mathavan S., Hussain G., Alkahtani M., Alqahtani F., Aboudaif M., 2021. A hybrid approach for noise reduction in acoustic signal of machining process using neural networks and ARMA model. *Sensors*. 21(23): 8023, http://doi.org/10.3390/s21238023.

Zhang C., Liang W., Li Z., Xu S., Zhao Y., 2015. Observations of acoustic emission of three salt rocks under uniaxial compression. *International Journal of Rock Mechanics and Mining Sciences.* 77,19-26. http://doi.org/10.1016/j.ijrmms.2015.03.030.

Zhang R., Dai F., Gao M., Xu N., Zhang C., 2015. Fractal analysis of acoustic emission during uniaxial and triaxial loading of rock. *International Journal of Rock Mechanics and Mining Sciences.* 79, 241-249. http://doi.org/10.1016/j.ijrmms.2015.08.020.

Zhang S., Li B., Xuan F., 2022. Signal denoising and classification prediction method for on-line monitoring of acoustic emission during laser melting process. *Journal of Mechanical Engineering.* http://kns.cnki.net/kcms/detail/11.2187.TH.20220526.1827.102.html. (In Chinese)

Captions for figures

1) Figure 1. Schematic diagram of the acoustic emission signal parameters.
2) Figure 2. Test equipment: (a) Electrohydraulic servo rock test system of RMT-150B. (b) Schematic diagram of uniaxial compression. (c) DS5-8B holographic acoustic emission signal analyzer. (d) Diagram of the sensor layout.
3) Figure 3. Uniaxial compression test results for the gypsum sample: (a) stress–strain curve. (b) The acoustic emission signal in Channel 1. (c) The acoustic emission signal in Channel 2. {The purple balls in three-dimensional space represent the ring-down count (N), while the cyan and pink balls are the projections of "N" on the (T_a, T_s) and (T_s, N) planes, respectively.}
4) Figure 4. Flow chart of the signal preprocessing procedure.
5) Figure 5. "Time of arrival" analysis of the two channel signals.
6) Figure 6. Preprocessing results of the acoustic emission signals.
7) Figure 7. Schematic diagram of the noise reduction according to the acoustic source distance and signal intensity.
8) Figure 8. Acoustic emission signal denoising processing based on the acoustic source distance: (a) The difference between the two channel signal intensity indices ($\triangle\lambda$). (b) The difference in moduli between the two channel signal intensity indices ($\triangle|\lambda|$). (c) The time difference between the two channels receiving the same signal ($\triangle T_a$).
9) Figure 9. Acoustic emission signal processing based on the acoustic source distance and intensity: (a) Diagram of the introduction of the i-axis. (b) Signal selection results.
10) Figure 10. Acoustic emission signal processing results based on the acoustic source distance and signal intensity.
11) Figure 11. Acoustic emission signal processing based on the acoustic source type: (a) Acoustic emission signal processing in Channel 1. (b) Acoustic emission signal processing in Channel 2.
12) Figure 12. Acoustic emission signal processing based on the acoustic source type: (a) $\sqrt{E}-T_s$ curve. (b) $\sqrt{E}-A$ curve.
13) Figure 13. Acoustic emission signal processing results based on the acoustic source type.
14) Figure 14. Analysis of the acoustic emission signal processing results: (a) Primary processing (acoustic source distance denoising). (b) Secondary processing (acoustic source type denoising). (c) Completion of processing.
15) Figure 15. Relationship between the acoustic source position and signal travel time.
16) Figure 16. Signal type and signal travel time: (a) Near range. (b) Long range.
17) Figure 17. Influence of the arrangement of the probe on signal noise reduction.

Captions for tables

1) Table 1: Acoustic emission parameters.

Captions for algorithms

1) Algorithm 1: Data grouping.
2) Algorithm 2: Comparison of data.
3) Algorithm 3: Determine the chronological order.
4) Algorithm 4: Eliminate the one-to-many case.